



# Deposition of highly crystalline AlScN thin films using synchronized high-power impulse magnetron sputtering: From combinatorial screening to piezoelectric devices

Jyotish Patidar <sup>1</sup>, Kerstin Thorwarth,<sup>1</sup> Thorsten Schmitz-Kempen,<sup>2</sup> Roland Kessels,<sup>2</sup> and Sebastian Siol <sup>1,\*</sup>

<sup>1</sup>*Empa, Swiss Federal Laboratories for Materials Science and Technology, Dübendorf 8600, Switzerland*

<sup>2</sup>*aixACCT Systems GmbH, Aachen 52068, Germany*



(Received 10 May 2024; accepted 12 August 2024; published 13 September 2024)

With the integration of 5G in day-to-day devices and the foreseeable 6G revolution, demand for advanced radio frequency (RF) microelectromechanical systems (MEMS) is growing. Aluminum scandium nitride (AlScN) has emerged as the material of choice for many of those applications due to its superior piezoelectric and electromechanical properties compared to aluminum nitride (AlN). However, synthesizing high-quality, textured AlScN thin films is challenging. Alloying of Sc in AlN induces structural frustration leading to strain, defects, disoriented grains, and disrupted crystal symmetry during growth. Higher deposition temperatures, while improving crystalline quality, risk undesirable phase precipitation and limit industrial sustainability. In addition, future MEMS technologies also demand conformal and textured coatings over diverse topographies. Addressing these challenges collectively requires new and innovative synthesis approaches. In this study, we investigate the feasibility of ionized physical vapor deposition to deposit highly oriented AlScN films with minimal defects at lower temperatures. To this end, we employ combinations of different deposition approaches, such as metal-ion synchronized (MIS) high-power impulse magnetron sputtering (HiPIMS). Leveraging the high ionization rates of HiPIMS and optimally timed substrate bias potentials, we selectively bombard the growing film with Al and/or Sc ions to enhance the adatom mobility at low temperatures while simultaneously providing the ability to tune stress and coat complex structures conformally. The nonequilibrium solubility of Sc in wurtzite AlN under different conditions is investigated using a combinatorial deposition approach. Promising candidates with  $\sim 20\%$  Sc composition are isolated and characterized for crystallinity and residual stress. Disoriented grains, a significant issue in growing AlScN films, are observed through atomic force microscopy and found to be completely removed by substrate rotation and application of substrate biasing. The measured piezoelectric response of the films with approximately 20% Sc concentration ranges from 6.3 to 8.8 pm/V, in line with density functional theory predictions and experimentally reported values for films deposited in a production tool with coplanar geometry. At the same time, MIS-HiPIMS-deposited films offer unique properties and flexibility to tune their stress state and structural properties, thus presenting exciting opportunities for the fabrication of advanced RF filters and next-generation MEMS devices.

DOI: [10.1103/PhysRevMaterials.8.095001](https://doi.org/10.1103/PhysRevMaterials.8.095001)

## I. INTRODUCTION

Fueled by recent advances in wireless communication, our interaction with technology has undergone a profound transformation. The higher frequencies and wider bandwidths associated with the current 5G and the forthcoming 6G standards necessitate the development of high-performance radio frequency (RF) filters. While these RF filters are predominantly used in the telecommunication industry, their applications extend to various emerging technologies, including unmanned drones, satellites, self-driving vehicles, wearables, and Internet of Things (IoT) applications. State-of-the-art filter designs are largely based on

piezoelectric microelectromechanical systems (MEMS). In RF filters based on MEMS acoustic resonators, the frequency and bandwidth of the filter critically depend on the properties of the underlying thin-film piezoelectric material. Aluminum nitride (AlN) in wurtzite structure has long been recognized as a valuable material in RF filters due to its linear frequency response and CMOS-compatible processing; however, it suffers from a comparably low piezoelectric response with low electromechanical coupling [1,2]. The addition of scandium (Sc) to the AlN lattice has been shown to introduce unique advantages, such as improved piezoelectric coefficients and enhanced electromechanical properties [3,4]. With their improved functional properties and the ability to tailor their characteristics through compositional and stress engineering, AlScN films have emerged as the material of choice for 5G RF components and are paving the way for exciting advancements in the field of piezoelectric MEMS [5–7].

The synthesis of aluminum scandium nitride (AlScN) films presents several challenges that need to be overcome to extract their full potential in piezoelectric applications. For piezoelectric applications, crystalline quality and texture are

\*Contact author: [sebastian.siol@empa.ch](mailto:sebastian.siol@empa.ch)

Published by the American Physical Society under the terms of the [Creative Commons Attribution 4.0 International](https://creativecommons.org/licenses/by/4.0/) license. Further distribution of this work must maintain attribution to the author(s) and the published article's title, journal citation, and DOI.

critical properties which affect device performance. To ensure a high average piezoelectric response, the films need to exhibit uniform *c*-axis texture and polarization. However, increasing the amount of Sc in the AlN lattice introduces structural frustration, causing local distortions, structural defects, and the growth of abnormally oriented grains [8–10]. Using high deposition temperatures can help in mitigating these defects; however, due to the high mixing enthalpy of wurtzite-AlN and cubic-ScN, this also promotes the precipitation of secondary phases [11,12]. In addition, the use of higher process temperatures on an industrial scale leads to higher production costs and reduced sustainability. Residual stress is another critical factor affecting the performance of RF-MEMS devices. In particular, stress can negatively influence the frequency response and mechanical integrity, emphasizing the importance of stress-free, crystalline, and uniformly textured AlScN films for commercial viability and device integration [13]. Co-optimizing these properties poses significant challenges for the process development.

Apart from the challenging synthesis of crystalline AlScN films with the aforementioned required properties, novel technologies in MEMS devices also require uniform coatings on parts with complex topographies such as cantilevers, resonators, microtrenches, three-dimensional (3D) electromechanical metamaterials, and so on [14,15]. Conformal deposition in trenchlike structures with texture along the substrate normal is of great interest in the MEMS industry right now to increase the active surface area of the piezoelectric materials. Atomic-layer deposition (ALD) and metalorganic chemical vapor deposition (MOCVD) are usually explored for such applications due to their ability to coat complex structures [16,17]. However, ALD processes typically feature low adatom kinetic energy and deposition rates, while MOCVD requires high growth temperatures, leading to high production costs. Thus, finding a novel deposition route that could provide conformal coatings irrespective of deposition angles and geometries, and that could surpass the drawbacks of ALD and MOCVD, would unlock a number of exciting new applications such as piezoelectric sensors or actuators on 3D-printed parts with complex shapes or on biomedical devices and wearables.

These challenges motivate the development of advanced deposition techniques, which enable the careful control of the growth parameters to achieve high-quality AlScN films with tailored structural and functional properties. The most common approaches to date to manufacture AlScN thin films at an industrial scale are direct current magnetron sputtering (DCMS) and pulsed direct current magnetron sputtering (pDCMS) from compound AlSc targets [18–20]. To unlock the full potential of AlScN films for future piezoelectric and ferroelectric applications researchers are continuously exploring alternative synthesis approaches and material engineering strategies [18,21–26]. In this regard, the development of ionized physical vapor deposition (IPVD) methods, such as high-power impulse magnetron sputtering (HiPIMS), and their use in the synthesis of functional films have picked up interest in the last few years [10,27,28]. Due to the inherently very high ionization rates of the process, the film-forming ions can be accelerated onto the growing film using substrate bias potentials, which helps in attaining high adatom mobil-

ity to deposit crystalline films at lower temperatures while simultaneously enabling conformal coverage over structured surfaces [29–34]. Despite these advantages, until now, HiPIMS deposition approaches have been predominantly used for hard coatings, optical coatings, or metallization [34–37]. The main reason for this is that thin films deposited by HiPIMS often exhibit defects and large residual stresses caused by process gas incorporation (typically Ar<sup>+</sup> ions), which limits their feasibility for defect-sensitive applications. These effects can be mitigated by the application of a novel metal-ion synchronized HiPIMS (MIS-HiPIMS) approach, which is based on the selective acceleration of the film-forming metal ions by applying a pulsed substrate bias synchronized to the metal-rich part of the plasma [28,38]. We recently demonstrated the deposition of out-of-plane (002) textured AlN films using metal-ion synchronized HiPIMS. By accelerating only the Al ions with low to moderate substrate bias potentials, remarkable improvements in the films' crystallinity and texture were achieved. The dense microstructure also resulted in a significantly improved resistance against bulk oxidation. Most importantly though, we could demonstrate that the new process design enables the deposition of highly textured films on structured surfaces and with shallow deposition angles [28]. These results highlight the potential of IPVD processes for the deposition of functional thin films, especially when highly textured and crystalline films are required. Consequently, such a deposition principle should be ideally suited to deposit high-quality AlScN thin films. To our knowledge, no synchronized HiPIMS deposition for AlScN has been reported to date.

The additional degrees of freedom during the reactive cosputtering of AlScN using IPVD techniques provide more flexibility for tuning the film's properties but also pose challenges in process optimization. Besides the conventional sputter process parameters, such as working pressure, nitrogen partial pressure, and sputter fluxes, reactive IPVD cosputtering with substrate bias synchronization opens up several new dimensions in the process parameter space. This necessitates a meticulous and mindful control of sputter conditions, which can greatly influence important film properties including structure, phase purity, and residual stress.

Of particular importance for AlScN thin-film development is the nonequilibrium Sc solubility in AlN, since higher Sc content has been shown to not only increase the piezoelectric response but also lower the coercive field for ferroelectric switching [39]. Despite its importance, only a few studies to date report on the experimentally determined nonequilibrium Sc solubility in AlN [3,12,40]. This is understandable, as traditional synthesis approaches require the deposition of many samples with varying compositions along with their individual structural analysis. A promising route to this challenge lies in the application of high-throughput experiments such as combinatorial screening [12,41]. Using gradient deposition, large areas of the synthesis phase space can be covered on a single materials library. Coupling this deposition approach with automated characterization and data analysis facilitates the rapid investigation of the phase constitution (i.e., the precipitation of secondary phases) and crystallinity as a function of composition for a given set of synthesis parameters.

In this work, we make use of such techniques to investigate the feasibility of different IPVD approaches to deposit

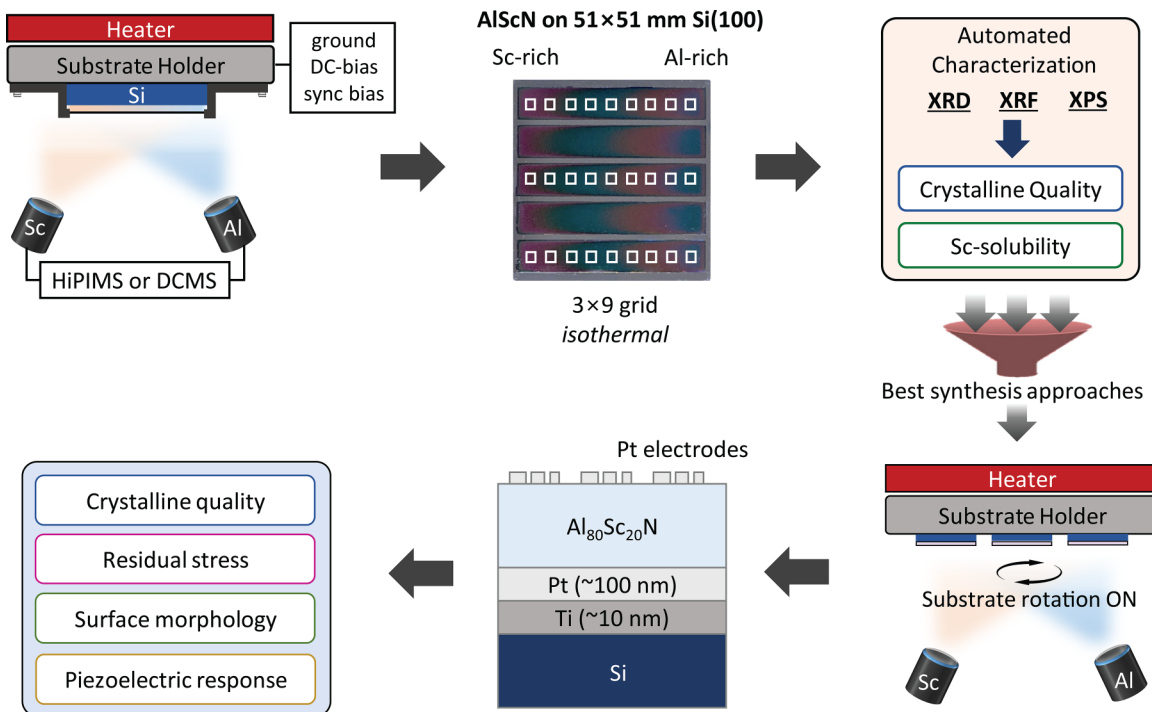


FIG. 1. Workflow used in this study. Combinatorial materials libraries are deposited on Si substrates for different combinations of sputtering modes and substrate biasing. The libraries are characterized using x-ray diffraction (XRD), x-ray fluorescence (XRF), and x-ray photoelectron spectroscopy (XPS) mapping to determine the relative crystalline quality and Sc solubility. Based on the most promising synthesis schemes from the combinatorial screening, single-phase  $\text{Al}_{80}\text{Sc}_{20}\text{N}$  films are synthesized and piezoelectric devices are fabricated with Pt top and bottom electrodes.

highly textured and crystalline AlScN films. The workflow of this investigation is shown in Fig. 1. Cosputtering from Al and Sc targets in a reactive atmosphere is performed using a hybrid deposition which employs different combinations of DCMS and/or HiPIMS. In addition, different biasing strategies are developed to probe the effect of low-energy ion bombardment on the crystalline quality and stress state of the films. A comparison of the crystalline quality and phase purity for a range of Sc compositions is performed based on an extensive combinatorial screening. Subsequently, based on the observed crystallinity and the Sc solubility limits, the most promising deposition schemes are chosen. Finally, for each approach, optimized single-phase films are deposited with approximately 20 at. % Sc. These films are characterized for their crystallinity, residual stress, surface morphology, and most importantly their piezoelectric coefficients ( $d_{33,f}$ ).

The results of this study clearly show that the added adatom mobility of the IPVD approaches does not only lead to highly oriented and crystalline AlScN thin films at moderate substrate temperatures. Moreover, the biasing of the substrate provides additional advantages like the removal of disoriented grains and the ability to tune stress by adjusting the kinetic energy of the film-forming species. In addition, despite the shallow deposition angle, the films show piezoelectric coefficients close to the current state of the art. At the same time, the deposition approach offers the promise of lower deposition temperatures and uniform deposition on structured surfaces, which could pave the way to exciting new applications and advanced RF-MEMS devices in the future.

## II. RESULTS

### A. Synchronization of the substrate-bias potential

During HiPIMS, following each sputter pulse, the different ionic species arrive at the substrate at different times. This is due to process-gas rarefaction and differences in ionic mass [42]. In metal-ion synchronized HiPIMS this phenomenon is leveraged by synchronizing a negative substrate-bias potential to selectively accelerate the film-forming metal ions, rather than the process gas ions. The goal is to deposit high-quality thin films at low deposition temperatures, while simultaneously minimizing process gas incorporation. For an effective synchronization, the time of flight (TOF) of the Al and Sc ions has to be known [28]. To this end, we performed time- and energy-resolved mass spectrometry using a Hidden Analytical EQP-300 placed at the working distance while facing the respective sputter guns. The measurements were performed for each ion species, including  $^{14}\text{N}$ ,  $^{36}\text{Ar}$ ,  $^{27}\text{Al}$ , and  $^{45}\text{Sc}$ . A less abundant isotope of Ar is used here to avoid the saturation of the detector. The TOF measurements along with the  $I$ - $V$  curves of the HiPIMS pulses are shown in Fig. 2.

In all experiments, the Sc and Al HiPIMS pulses start at the same time (i.e., 0  $\mu\text{s}$ ). It is apparent from the TOF measurements that the Ar ions arrive predominantly in the first 15  $\mu\text{s}$  after the initiation of the HiPIMS pulses, whereas the Al and Sc ion fluxes reach peak intensity at 25 and 30  $\mu\text{s}$ , respectively. We find that applying a 40- $\mu\text{s}$  substrate-bias pulse with a time delay of 20  $\mu\text{s}$  effectively accelerates both Al and Sc ions while avoiding acceleration of the process gas ions. A moderate potential of  $-30$  V is chosen to achieve

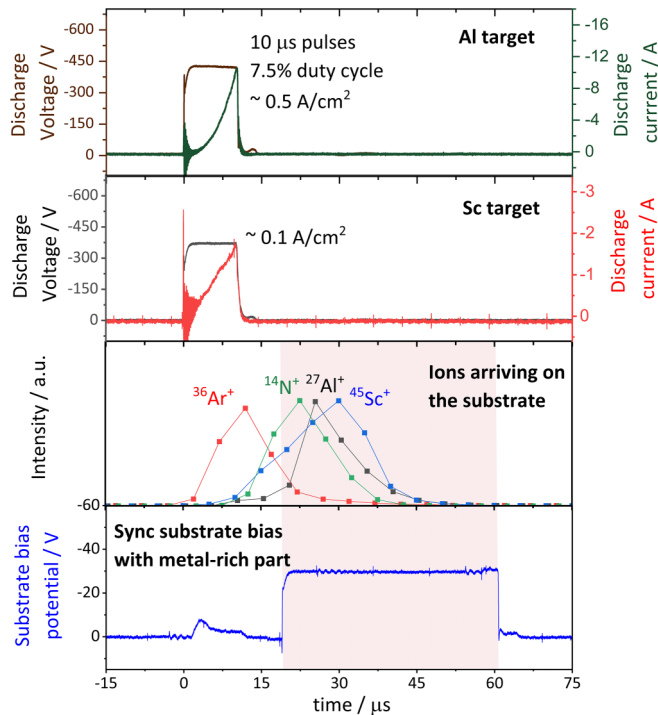


FIG. 2. Synchronization of substrate-bias pulse with the metal-rich part of HiPIMS plasmas. The pulses on Al and Sc targets are also synchronized to start at the same time.

a median ion kinetic energy below the lattice displacement threshold [28]. The motivation behind this approach is to provide a low-energy metal-ion bombardment while simultaneously avoiding ion implantation, which could lead to structural defects and excess compressive stress.

### B. Combinatorial screening of deposition modes

The reactive cosputtering of AlScN with synchronized IPVD processes poses significant challenges to process development due to the vast synthesis parameter space. In this study, we try to investigate the feasibility of different principle deposition modes for the deposition of high-quality AlScN thin films with the help of combinatorial high-throughput experiments. For the films' deposition, the Al and Sc sputter guns were operated in multiple combinations of sputtering modes, namely, HiPIMS-AIN/DCMS-ScN, DCMS-AIN/HiPIMS-ScN, DCMS-AIN/DCMS-ScN, and HiPIMS-AIN/HiPIMS-ScN. These modes correspond to ionizing different fractions of the sputter flux, i.e., Al, Sc, or both Al and Sc. For the substrate, different biasing strategies are evaluated. These include a grounded substrate (no additional acceleration), a constant bias of  $-30$  V (a constant acceleration of all ions, including  $\text{Ar}^+$ ), or a synchronized bias pulse of  $-30$  V (selective metal-ion acceleration).

For each combination of deposition modes several combinatorial materials libraries were deposited, covering a wide range of Sc alloying concentrations. In total over 200 unique samples were tested. The samples were evaluated for crystalline quality and phase constitution through automated x-ray diffraction (XRD) analysis. The full width at half maximum

(FWHM) of the (002) AlScN peak serves as an indicator of grain size and, consequently, is utilized as a measure of the films' crystalline quality. It is important to note that this assessment is qualitative, since the FWHM obtained here could be affected by a convolution of several parameters. In addition, the FWHM can be substantially changed with film thickness, and thus it is ensured that the thicknesses of libraries are similar for fair comparison. Figure 3 illustrates the FWHM values for all examined samples in the combinatorial libraries, organized based on decreasing solubility limits from Fig. 3(a) to Fig. 3(g). The solubility limit is calculated by evaluating the phase purity of w-AlScN films through XRD  $\theta$ - $2\theta$  screening based on the emergence of the c-ScN phase with varying Sc concentration. It is well known that for DCMS depositions at oblique angles, the films preferentially grow in the direction of the sputter source, according to the tangent rule [43,44]. This phenomenon was evident in the combinatorial screening, where the flux from the sputter gun connected to DC power supplies promoted the growth of the respective phase in the direction of the deposition flux. Thus, it is critical to look for secondary phases with the help of  $\chi$  scans to avoid an overestimation of the phase purity and solubility limits. The procedure for determining the solubility limits is illustrated in detail in Supplemental Material Sec. S1 [45].

The solubility limit is marked by a red dotted line in Fig. 3. Pronounced precipitation typically leads to higher leakage currents and reduced crystallinity, which can negatively affect device performance. A more direct correlation exists between the structural properties and the piezoelectric response in AlScN. For this reason, the region below the FWHM of  $0.5^\circ$  is marked green and labeled as the region of interest. The range of interest (FWHM from  $0^\circ$  to  $0.5^\circ$ ) chosen is relatively generous here since the grain size of the films will certainly increase with substrate rotation and optimized synthesis parameters for single-phase samples. As anticipated, the FWHM of AlScN notably increases beyond the solubility limit for all deposition modes. Strikingly, some deposition modes [see Figs. 3(e)–3(g)] seem less susceptible to this degradation. This is likely due to the increased ion bombardment, particularly when applying substrate biasing, which leads to higher adatom mobility, which helps in keeping the structural integrity intact even after slight precipitation. Films deposited using DC on both sputter guns exhibited markedly higher FWHM due to lower ionized flux and the inherent low adatom mobility. The introduction of ion bombardment, facilitated by HiPIMS on either or both sputter guns, demonstrated improved crystalline properties irrespective of substrate biasing. The percentage of ion flux in the HiPIMS mode for each sputter gun was calculated for both Al and Sc by depositing the films with a grounded substrate and with a positive bias [46]. The ion-to-neutral flux was then calculated by taking the ratio of the difference in thickness of the film with and without bias. The resulting ion fluxes for Al and Sc in HiPIMS mode at  $0.5$  and  $0.1$   $\text{A}/\text{cm}^2$  were found to be approximately 30% and 9%, respectively. The ionization fraction of Sc plasma is relatively lower, primarily due to the constraints imposed by the sputter power limitations to achieve lower alloying percentages. Although Sc in HiPIMS modes provides a lower ion-flux density, the ion mass and therefore the momentum transfer to the growing film is higher when compared to Al.



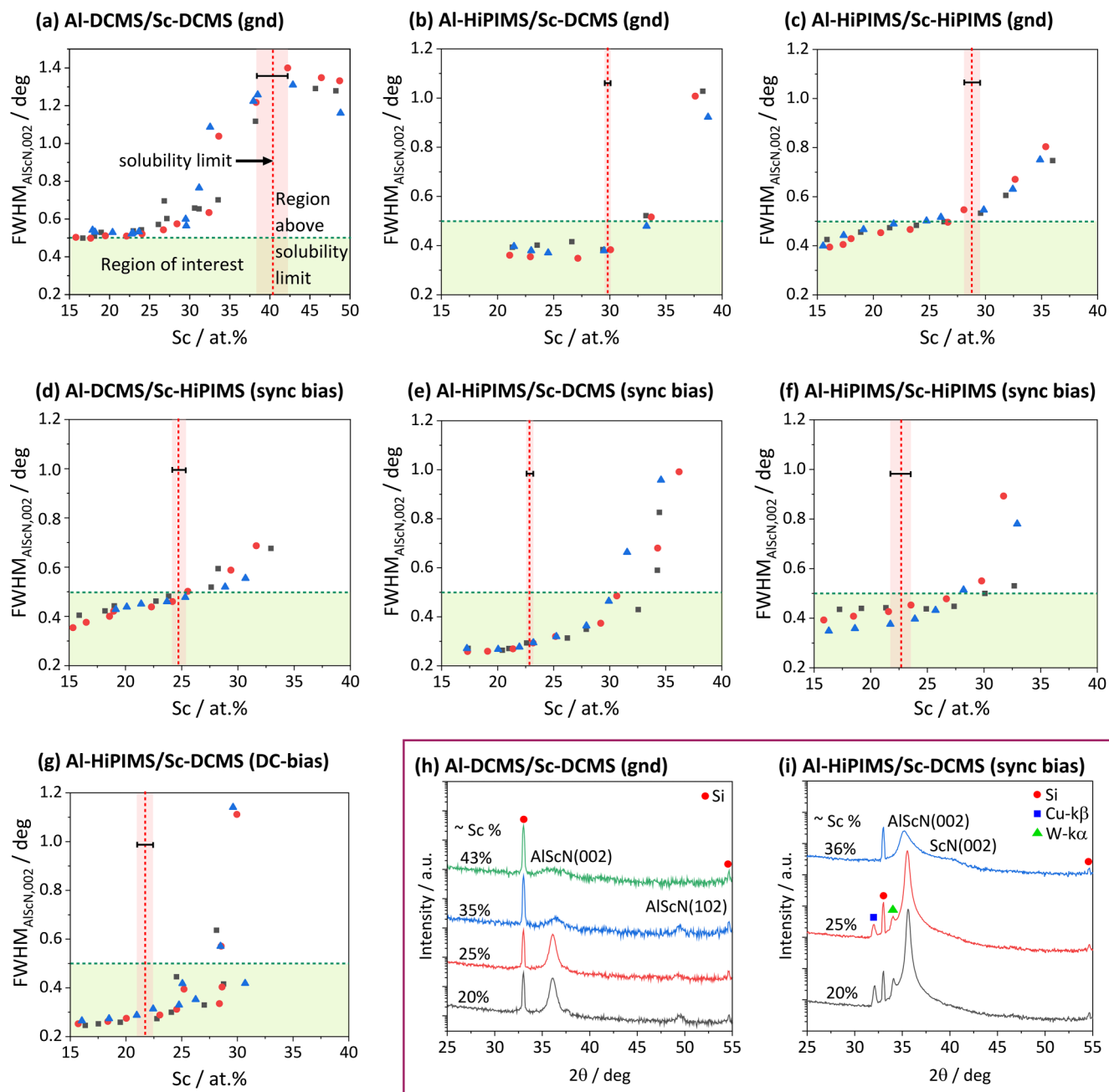


FIG. 3. Relative comparison of crystalline quality and estimation of solubility limits of AlScN combinatorial libraries. The combinatorial libraries are deposited for different combinations of sputter modes and substrate biasing approaches [labeled in respective plots (a)–(g)]. The FWHM of the AlScN (002) reflection is used as a proxy for the grain size. The red line marks the first detectable precipitation of c-ScN. To illustrate the formation of precipitates, the XRD patterns of films deposited with Al-DCMS/Sc-DCMS (ground) and Al-HiPIMS/Sc-DCMS (sync bias) are stacked for different Sc composition in panels (h) and (i), respectively.

Consequently, no significant difference in film quality was observed when comparing selective Al- or Sc-ion irradiation of the growing film. A more pronounced difference was observed for the different substrate biasing modes. In particular, films with Al in HiPIMS mode and Sc in DCMS mode showed an increase in crystallinity with the application of a substrate bias. The acceleration of Sc ions appears to be detrimental, which could be due to the higher mass and consequently higher momentum transfer to the growing film. In addition to changes in grain size a lower Sc solubility limit was observed

with the application of substrate biasing. Here films with DC substrate bias exhibited the lowest Sc solubility.

Overall, the grain size of HiPIMS-deposited films was far superior compared to the DCMS deposition [Fig. 3(a)]. In addition, the AlScN grain orientation varied across the library in the direction of sputter flux, as confirmed by XRD. This is likely a result of the shallow deposition angles in our confocal sputter chamber geometry combined with the moderate substrate temperature used in this study [28]. These results underline that for best results during DCMS of AlScN thin

films on-axis deposition at higher deposition temperatures is necessary [47,48]. Considering these factors, we focus on the following detailed characterization of the films deposited with IPVD approaches.

### C. Properties of HiPIMS-deposited $\text{Al}_{80}\text{Sc}_{20}\text{N}$ thin films

#### 1. Morphology and abnormally oriented grains

Given that the solubility limits for all examined samples exceeded 20%, we decided to deposit AlScN films with a homogenous Sc concentration of 20% for all promising deposition schemes for further investigation. At first, we investigated the microstructures of films deposited with Al-HiPIMS/Sc-DCMS with grounded and synchronized substrate biases. Figure 4 shows atomic force microscopy (AFM) images for films deposited without substrate rotation [Figs. 4(a) and 4(b)], with substrate rotation [Figs. 4(c) and 4(d)], and with substrate rotation on a Ti/Pt bottom layer [Figs. 4(e) and 4(f)]. The triangular-appearing structures protruding out from the surface in the images are abnormally oriented grains (AOGs), which diverge from the otherwise uniform texture. AOGs are typically formed due to *c*-axis instability occurring during growth in which the cubic ScN nuclei get incorporated in the (002) AlScN wurtzite crystal during growth. Over time, Al gets incorporated in the *c*-ScN crystallites, prompting it to revert to the wurtzite phase. This transformation results in the loss of original orientation and the formation of tilted AOGs [8]. The AOGs are not aligned with the rest of the grains and thus lower the overall piezoelectric performance of the film. With increasing thickness, these grains enlarge and take up large fractions of the film volume. Therefore, it is important to address the formation of these grains and ways to prevent their nucleation. The AOGs are more prominent in films deposited without rotation, contrary to other films. This is primarily because of the shadowing effect caused by protruding AOGs, which leads to further accumulation of Sc at the protruding grain boundaries. Strikingly, the AOG can be completely obliterated with the application of substrate biasing (sync or DC), due to increased adatom mobility and compressive stress in the film [49]. High adatom mobility allows the atom to arrange in low-energy basal planes, avoiding the nucleation of disoriented grains in other directions. On the other hand, compressive stress in the film suppresses the growth of AOGs by densifying the film. Both factors have been shown to be effective in the removal of these grains; however, it is difficult to pinpoint which factor is more prominent here. Previous studies have demonstrated that the bottom Pt layer also plays a role. Here epitaxial matching of AlScN(002) and Pt(111) occurs when the *w*-AlScN crystal is rotated 30° along the *c* axis relative to the Pt(111) template [50]. Thus, in order to facilitate piezoelectric measurements and enhanced nucleation, the isolated films were grown on a 100-nm-thick Pt layer for further investigations (see Fig. 1). With Pt as a bottom layer, the enhanced nucleation can be seen with the enlargement of grains of the film. The pronounced nucleation with the help of the Pt layer in combination with substrate rotation and biasing can help in obtaining crystallized films with no AOGs.

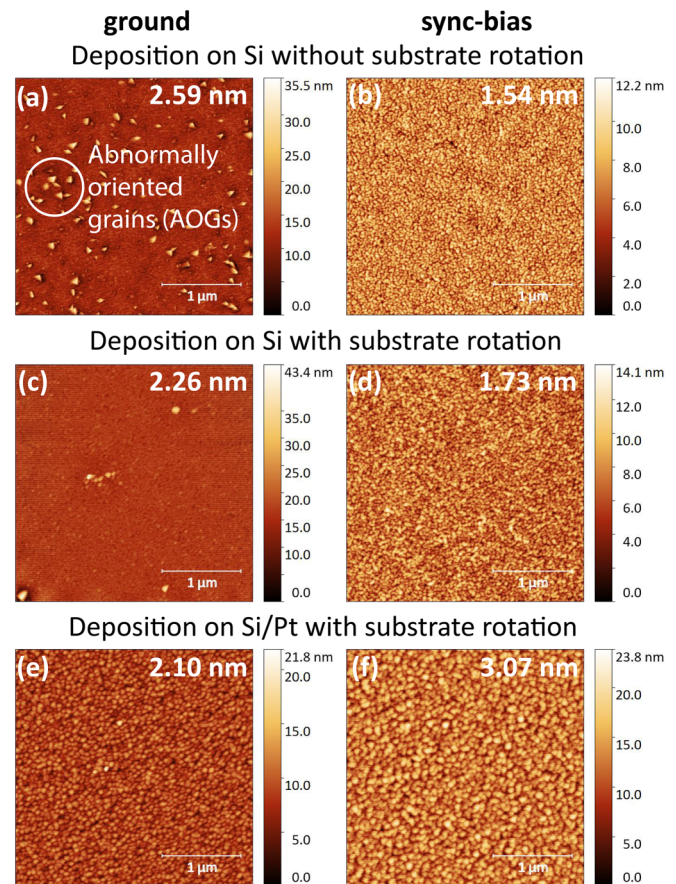


FIG. 4. AFM imaging of  $\text{Al}_{0.8}\text{Sc}_{0.2}\text{N}$  films deposited with the grounded and sync-bias approach for substrate rotated and still during the deposition. The images show changes in the formation of abnormally oriented grains as well as the RMS surface roughness. The shadowing effect, prominent when the substrate is stationary, increases Sc accumulation over grains. Rotating the substrate during deposition helps mitigate this effect. In addition, the high adatom mobility of atoms and compressive stress induced by ion bombardment also suppress the growth of AOGs.

#### 2. Residual stress and texture

Following the combinatorial screening, we proceeded to investigate isolated films with a homogeneous 20% Sc concentration concerning their residual stress and out-of-plane texture. The films investigated here showed no detectable oxygen contamination even after exposure to air due to their compact microstructure (see Supplemental Material Sec. S2) [45]. The data for all samples, along with the solubility limits estimated from combinatorial screening, are plotted in Fig. 5(a) and arranged in order of stress (estimated using the XRD wafer curvature method) from tensile to compressive (left to right). The films exhibit similar thicknesses ranging from 650 to 750 nm. All the films were completely textured and highly crystalline, which was verified from the XRD patterns and pole figures in Supplemental Material Sec. S3 [45]. For comparison, data for AlN films deposited using HiPIMS with grounded and synchronized biasing are also discussed. Strikingly the residual stress changes significantly for different deposition schemes, which results in more or less

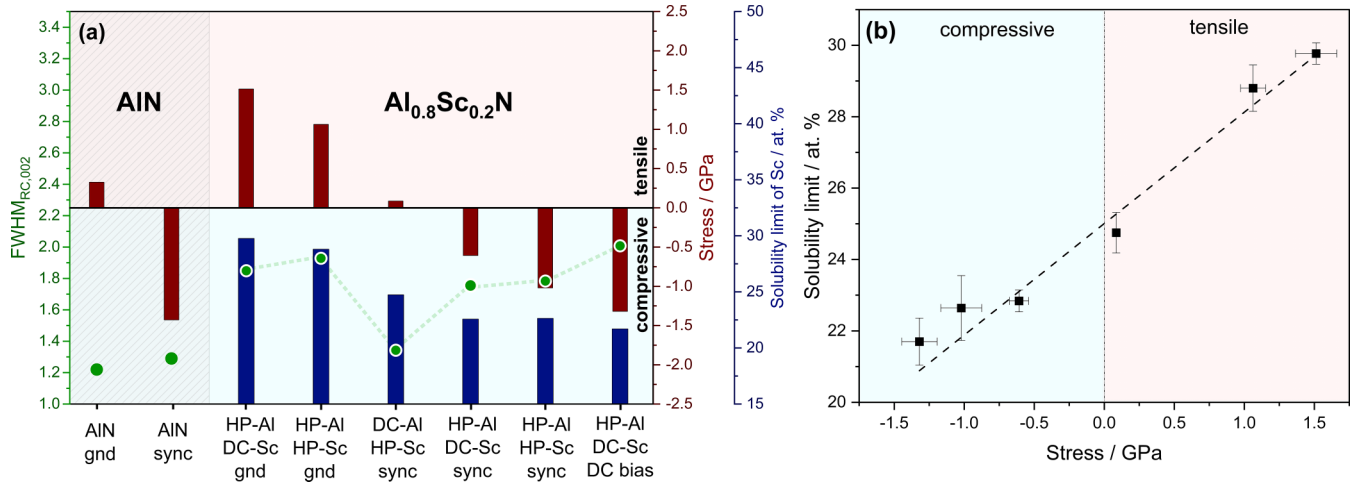


FIG. 5. (a) Plot summarizing the FWHM of the rocking curve, residual stress, and solubility limit estimated from combinatorial screening for AlN and AlScN films deposited with different combinations of power supplies and substrate biasing. Here HP and DC are used as abbreviations for sputter guns operated in HiPIMS and DCMS mode, respectively. (b) Change in solubility limit with stress obtained for films discussed in (a).

energetic ion bombardment. This highlights the ability to tailor stress in the films by adjusting the HiPIMS deposition parameters and the respective ion acceleration. The most pronounced out-of-plane texture is observed for films with no or slight tensile stress. The FWHM of the rocking curve evidently increases with the residual stress in the film, regardless of whether it is tensile or compressive. This is attributed to the dislocations, grain elongation, and microstructural defects caused by increased stress in the system.

In addition to changes in the out-of-plane texture, we observe a strong correlation of the films' stress with the estimated solubility limits from the combinatorial screening of the libraries of respective deposition schemes. In Figs. 5(a) and 5(b), the solubility limit from combinatorial screening can be seen to vary linearly with the residual stress of the film. The effect of stress on the maximum solubility of cubic systems in wurtzite has also been studied earlier based on *ab initio* thermodynamic and kinetic models for other material systems such as AlTiN, AlVN, and AlCrN [51,52]. Residual stress, deposition rates, and thermodynamic and kinetic factors have been found to be the driving factors for the variation in solubility observed in these systems. Greczynski *et al.* reported the variance of maximum solubility by subplantation of energetic metal ions onto the high-mobility surface zone of the growing film [53]. However, due to the low substrate bias potentials chosen in this investigation, particularly to avoid the formation of defects and large compressive stresses, the effect of ion subplantation is not dominant and can be ruled out. Deposition rate and microstructural effects can also play an important role in determining the maximum solubility of the system. All investigated films exhibit similar compact columnar microstructure and deposition rates, except the film deposited in purely DCMS mode, which tends to have a columnar structure with open grain boundaries [28]. The presence of high compressive stress leads to a densification of the film, thereby favoring the formation of a more compact cubic lattice. Thus, it leads to reduced maximum solubility of

Sc lattice in wurtzite AlN, i.e., precipitation of c-ScN at lower Sc concentrations. From our investigation we conclude that, for films exhibiting compact microstructures, intrinsic stress is the main driving force for the variation of the solubility limits.

### 3. Piezoelectric response

Subsequently, we measured the piezoelectric response of the above-discussed films and determined the clamped piezoelectric coefficients,  $d_{33,f}$ . The measurements were performed using double-beam laser interferometry (DBLI) at aixACCT GmbH. The reported values measured with this technique tend to be slightly lower than those measured with mechanical methods (e.g., Berlincourt method) [54]. DBLI is considered one of the most accurate characterization techniques for piezoelectric thin films as it fully accounts for the deformation of the substrate during actuation [55].

The measured piezoelectric coefficients for the HiPIMS-deposited AlScN are plotted in Fig. 6 along with comparable DBLI measured experimental values obtained from the literature and density functional theory (DFT) predictions from Caro *et al.* [56–58]. In addition, we report  $d_{33,f}$  values for AlN films [28]. To our knowledge, these are the first reported piezoelectric coefficients for AlN and AlScN films deposited with HiPIMS processes. The  $d_{33,f}$  of AlN films deposited with HiPIMS were found to vary from 3.59 to 3.92 pm/V, while the  $d_{33,f}$  of AlScN films varied from 6.31 to 8.81 pm/V. Strikingly, despite the shallow sputter angles and high working distances, the response of our HiPIMS-deposited films is on par with experimental values by Mertin *et al.* and Tsubouchi *et al.* [56,57]. This is particularly interesting as these reference values were achieved using coplanar deposition geometry (i.e., on-axis sputtering at low working distances) in an industrial sputter coater, closely resembling the current state of the art in the industry.

Some minor differences in the response are observed among the HiPIMS-deposited films. It is interesting to note



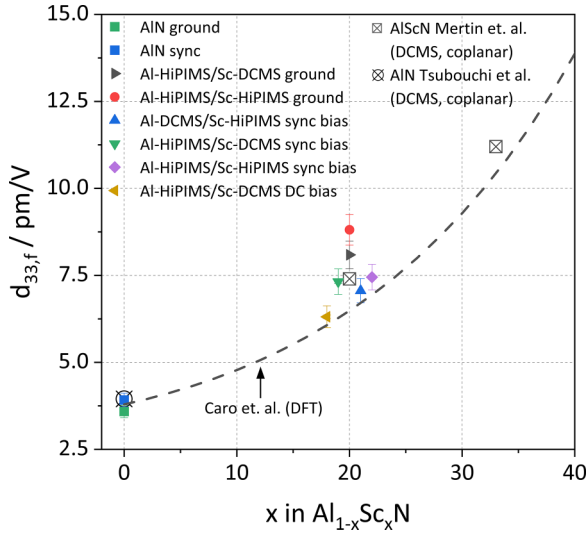


FIG. 6. Piezoelectric coefficient  $d_{33,f}$  for investigated  $\text{Al}_{0.8}\text{Sc}_{0.2}\text{N}$  samples along with DFT predictions and experimental values reported in the literature. The  $d_{33,f}$  values closely match with the DFT predictions [58] and experimental values of samples deposited in coplanar geometry [56,57].

that the piezoelectric coefficients of the films are not overly sensitive to residual stress. Since all the investigated films were relatively well oriented in the  $c$  axis, the effect of crystallinity on piezoelectric coefficients is not pronounced. On a closer look, the  $d_{33,f}$  of all metal-ion-synchronized films are minutely lower than the ones with the grounded substrate, while the one with DC bias is even lower than the sync-bias samples. The effect is very little, presumably due to the gentle conditions used for the deposition of these functional films. It is speculated that the minute decrease in the coefficients could be due to the formation of point defects in the films due to substrate biasing and compressive stress. This effect of stress on the piezoelectric response has also been observed by researchers earlier [59,60]. On the other hand, the use of synchronized biasing offers the advantages of tuning the stress state of the film along with its application to coat structured surfaces or deposition of these functional films in oblique deposition geometries. The ability to deposit high-quality piezoelectric thin films at shallow deposition angles and moderate temperatures demonstrates the great potential of IPVD processes for functional defect-sensitive coatings.

#### 4. Deposition on structured surfaces

The HiPIMS technique, combined with a sync substrate biasing approach, offers a convenient method for depositing films on complex structures by deflecting ions towards the substrate and increasing the adatom mobility. While this technique has long been utilized by the industry for depositing hard coatings in microtrenches and 3D structures, its application in growing crystalline functional coatings has not been explored yet [61,62]. Thus, to verify the conformal growth of crystalline AlScN films over structured surfaces, we deposited a 150-nm-thick film on an etched Si wafer with pyramids featuring facets in the [111] direction. The Al target was positioned under the substrate and operated in HiPIMS mode,

while Sc was deposited using two sputter guns at an oblique angle operating in DCMS mode (see Supplemental Material Sec. S4 [45]). A synchronized substrate-bias potential was applied. The substrate was rotated throughout the deposition process to ensure uniform Sc alloying and conformal deposition. This setup was intentionally chosen to ensure the continuous arrival of Al and Sc flux at the substrate, mitigating the potential formation of stacked AlN and ScN layers due to shadowing effects that could occur if both Al and Sc were operated at oblique angles.

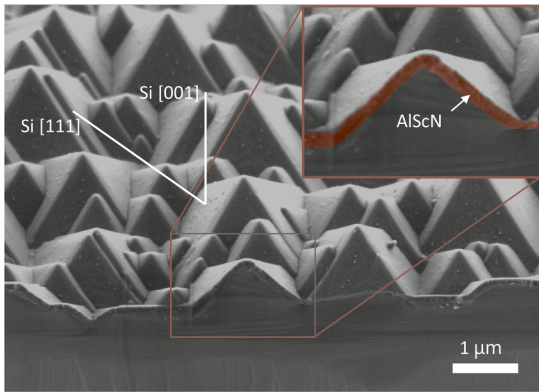
The scanning electron microscopy (SEM) cross sections in Fig. 7(a) illustrate the uniform growth of the film, with the pyramids maintaining their shape even after film deposition, indicating consistent film growth over the facets. To assess the texture of the films over the pyramids, pole figure measurements were conducted on the bare Si substrate and on the coated substrate, as shown in Fig. 7(b). The Si(111) pole figure shows sharp peaks at four points corresponding to the four facets of the pyramids, and similarly, the AlScN film grown over these facets also shows four corresponding points on the pole figure indicating growth of  $c$ -axis-oriented films on all four facets. Only a slight difference of about  $5^\circ$  in  $\chi$  between the Si(111) and AlScN(002) suggests a minor misalignment of grains relative to the facets' normal. In the future, this misalignment could be further reduced by sputtering from a compound target in coplanar geometry and further optimization of the substrate-bias potential pulse pattern.

### III. CONCLUSION

The demand for MEMS thin films with tailored functionality is increasing rapidly. Future applications will include increasingly complex sample geometries and constraints for deposition temperatures. It has recently been shown that metal-ion synchronized HiPIMS can offer significant advantages for the deposition of highly textured thin films at moderate temperatures, even at shallow deposition angles or on structured surfaces [28]. In this study, we investigated the feasibility of this concept for the reactive cosputtering of AlScN and particularly for the fabrication of piezoelectric devices. To this end, different combinations of sputtering modes (DCMS and/or HiPIMS) along with varying substrate-biasing approaches (ground, DC bias, sync bias) were tested. For a rapid screening of the synthesis parameter space, a combinatorial synthesis with automated characterization and data analysis was employed. The combinatorial screening helped assess the relative crystallinity of films and of the solubility limit of Sc for a number of different synthesis approaches. This screening showed a significant improvement in crystallinity for HiPIMS approaches compared to conventional sputtering, at the cost of Sc solubility. Based on this screening, single-phase  $\text{Al}_{0.8}\text{Sc}_{0.2}\text{N}$  films were deposited on smaller Si substrates with homogenous composition for promising conditions. It was found that the growth of AOGs can be suppressed by substrate rotation and application of negative biasing on the substrate. Detailed analysis of the structural properties revealed that the stress state of the films can be tuned over several GPa using a combination of HiPIMS deposition and substrate biasing. Strikingly, a direct correlation between the maximum solubility of Sc and the residual stress



(a) Growth on structured Si substrates



(b) AlScN (002) and Si (111) pole figures

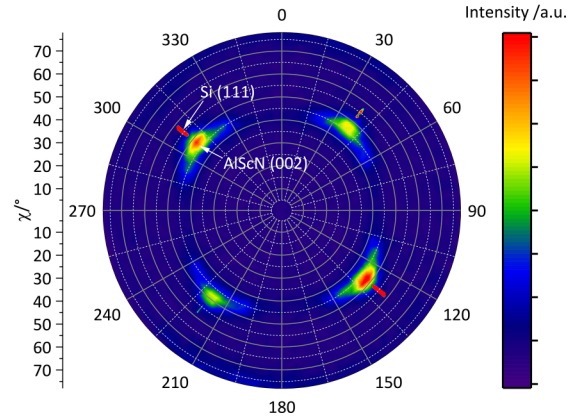


FIG. 7. (a) SEM cross section of AlScN films grown on structured Si wafer. The wafer has micro-sized pyramids with [111] facets formed by chemical etching of a [001] wafer. The cross section reveals a uniform film thickness. (b) XRD pole figure measurement on AlScN (002) confirms that the films grow with a pronounced  $c$ -axis texture on the [111] facets of the pyramids, confirming that the films' texture is maintained even at shallow deposition angles.

in the films was established. Here, we find that the compressive stress leads to the densification of the film and a change in the  $c/a$  ratio in the hexagonal lattice of  $w$ -AlScN, ultimately resulting in the precipitation of the denser  $c$ -ScN phase. Finally, the piezoelectric response was investigated on thin-film device structures using DBLI. Despite the nonoptimized chamber geometry (i.e., shallow deposition angles and high working distances), the piezoelectric coefficient  $d_{33,f}$  was found to be on par with the current state of the art achieved in production systems. The  $d_{33,f}$  shows similar values for all HiPIMS approaches. Although all the films exhibited similar piezoelectric responses varying from 6.3 to 8.8 pm/V, the films deposited with sync bias provide us with an opportunity to tune the stress of the system, deposit films with compact microstructure, and provide the ability to coat structured substrates. The conformal coverage of AlScN films over a structured Si wafer was further confirmed with the help of SEM imaging, and pole figure measurements confirmed  $c$ -axis-oriented growth on the [111] facets of the pyramid structure. Overall, the results of this study demonstrate the potential of advanced IPVD approaches like MIS-HiPIMS for next-generation MEMS technologies. Implementing such deposition techniques might enable exciting new applications for piezoelectric and ferroelectric thin films in the future, in particular for applications requiring low substrate temperatures or devices with complex geometries.

#### IV. EXPERIMENTAL DETAILS

AlScN films were deposited using a custom-built sputter chamber (AJA International, ATC-1800), with a base pressure of  $<10^{-6}$  Pa. The films were deposited on p-type Si (100) wafers with unbalanced magnetrons equipped with 2-in. Al (Lesker, purity 99.999 at. %) and Sc target (Plasmaterials, purity 99.9 at. %; Hunan Advanced Metal Material Co. Ltd, purity 99.9 at. %, O  $< 800$  ppm). The magnetrons were aligned with a sputter angle of  $26^\circ$  with respect to the substrate normal and the working distance was set at 12 cm. A closed-field magnetic configuration was used between the

opposite magnetrons to reduce the amount of plasma heating [28,63,64]. Nitrogen was routed directly to the targets to ensure easier poisoning of the targets while the Ar gas was supplied away from the target in the chamber. The flow rates of Ar/N<sub>2</sub> and working pressure are maintained constant at 20 and 12 sccm, respectively. The depositions were performed at  $300^\circ\text{C}$  and at a working pressure of 3.5 Pa. The substrate holder is heated from the back using five halogen lamps, resulting in homogenous heat distribution across the holder. The substrate is maintained at a constant temperature of  $300^\circ\text{C}$ . Before the deposition the Si substrates are etched by RF Ar plasma at 30 W for 8 min to remove the native oxide layer. The power and current densities for DCMS and HiPIMS for each sputter gun are summarized in Table I. The substrate holder is either grounded or negatively biased depending on different deposition approaches, which are described further in this section.

For the synchronization of the substrate bias, the time of flight of the Al and Sc ions was first estimated by time-resolved mass spectrometry measurement using a Hidden Analytical EQP-300. The orifice of the spectrometer, 50  $\mu\text{m}$  in diameter, was grounded and placed at the working distance while facing the sputter gun. The triggering signal was provided by the pulsing unit of the HiPIMS power supply attached to the target. The gate width was set to 5  $\mu\text{s}$ , consistent with the step size of measurement. The time-resolved measurements were performed for each ion species, including  $^{14}\text{N}$ ,  $^{36}\text{Ar}$ ,  $^{27}\text{Al}$ , and  $^{45}\text{Sc}$ . A less abundant isotope

TABLE I. Power and current densities for Al and Sc sputter guns operated in DCMS and HiPIMS modes.

	Power density ( $\text{W}/\text{cm}^2$ )	Current density ( $\text{mA}/\text{cm}^2$ )
Al-DCMS	6	23–26
Al-HiPIMS	5	450–550
Sc-DCMS	0.85	3.5–5.5
Sc-HiPIMS	$\sim 1.5$	100–150

of Ar is used here to avoid the saturation of the detector. The time of flight in the mass spectrometer is calibrated by applying a gating potential at the driven front end of the spectrometer. A more detailed description of this method can be found in our previous publication [28].

For the films' deposition, the Al and Sc sputter guns were operated in multiple combinations of sputtering modes, namely, HiPIMS-AIN/DCMS-ScN, DCMS-AIN/HiPIMS-ScN, DCMS-AIN/DCMS-ScN, and HiPIMS-AIN/HiPIMS-ScN. DCMS is carried out using a 750-W DC power supply by AJA International (DCXS 750). HiPIMS is carried out using Ionautics pulsing units and power supplies (HiPSTER 1 bipolar). The 10- $\mu$ s HiPIMS pulses with a frequency of 7.5 kHz on the targets were synchronized to start at the same time using an Ionautics synchronization unit.

For the substrate, different biasing strategies are evaluated. These included a grounded substrate, a constant bias of  $-30$  V (DC bias) or a synchronized bias pulse of  $-30$  V. In the latter mode, the substrate pulse was synchronized to the metal-rich part of the plasma. Specifically, a 40- $\mu$ s substrate bias pulse of  $-30$  V is applied with an offset of 20  $\mu$ s using the same bipolar HiPIMS power supply and is actively regulated to 0 V between the pulses. The synchronization scheme with the  $I$ - $V$  curve of the HiPIMS discharges is shown in Fig. 2.

For the combinatorial depositions, the films were deposited without substrate rotation on a  $2 \times 2$  sq in. Si (100) wafer, thus obtaining a compositional gradient on one axis. The wafer was clamped uniformly to the holder with additional masks to homogenize the temperature throughout the wafer. Each combinatorial library has three rows with each row consisting of nine samples with increasing composition of Sc in one direction, thus giving 27 samples in total for one deposition, as illustrated in Fig. 1. The data from multiple rows are investigated in order to rule out geometric effects from localized plasma heating. Based on the results from the combinatorial studies, the promising set of conditions was chosen for deposition of isolated samples on smaller  $13 \times 13$  mm<sup>2</sup> double-side polished Si (100) wafers. The isolated samples were deposited for a fixed Sc composition of  $\sim 20 \pm 2$  at. % with substrate rotated at 40 rpm. The stack of layers is illustrated in Fig. 1 for these samples. A 10-nm Ti layer acts as an adhesion layer and also prevents the formation of PtSi at the interface. The Pt layer over it acts as a bottom electrode for piezoelectric measurements and also enhances the nucleation due to the epitaxial relationship and reduced lattice mismatch in comparison to the Si lattice [50]. Then the top electrode pads were deposited over the AlScN and AlN films with the help of a shadow mask with square pad areas of 0.16, 0.36, and 0.64 mm<sup>2</sup>. The films used for the fabrication of piezoelectric devices showed no detectable oxygen contamination [measured via x-ray photoelectron spectroscopy (XPS) depth profiles] even after exposure to air due to their compact microstructure. The AlScN films deposited with a lower-purity Sc target exhibited approximately 2–3 % bulk oxygen, resulting in a slightly reduced piezoelectric coefficient. These films are not further discussed in the main text and the  $d_{33,f}$  comparison of samples with and without oxygen, along with XPS depth profiles of these films, can be found in the Supplemental Material Sec. S2 [45] (see also Refs. [65,66] therein). Finally, AlScN film was also deposited

on an etched Si wafer, with pyramid facets in the [111] direction.

XRD analysis of the films was performed using a Bruker D8 in Bragg-Brentano geometry and Cu  $K\alpha$  radiation. The estimation of crystalline quality and solubility limit was done for the combinatorial libraries using automated XRD  $\theta$ - $2\theta$  measurements. The composition of the combinatorial libraries and films was estimated using automated x-ray fluorescence (XRF) measurements. The XRF data for the chemical composition of films was calibrated based on the composition obtained through XPS (PHI-Quantera, Al  $K\alpha$  radiation) for a few combinatorial libraries transferred in UHV conditions directly after the deposition to the XPS. The large data sets were then analyzed using the CombIgor data analysis package in Igor Pro software. The morphology and disoriented grains present in the films were visualized using Bruker nanoscope AFM. The measurements were done in ScanAsyst mode with silicon cantilever tips.  $3 \times 3$   $\mu$ m<sup>2</sup> AFM images with a pixel resolution of  $512 \times 512$  were captured using Nanoscope software and later processed in Gwyddion. The thickness of the films was measured using a Dektak profilometer. The residual stress in the films was calculated using the wafer curvature method, by measuring the peak position of the Si(100) peak via rocking curve measurements at several positions on the wafer. Stoney's equation was used further to calculate the residual stress in the films. The equation and coefficients used for the calculation can be found in Supplemental Material Sec. S5 [45,67].

The piezoelectric response of the fabricated layer stacks on the double-side polished Si(100) wafers was measured using DBLI by aixACCT GmbH. This method uses laser interferometry to measure not only the surface displacement, but the expansion of the whole layer stack relative to the applied potential. This way, the bending of the substrate is taken fully into consideration. Measurement configurations with one laser interferometer, or mechanical testing setups (e.g., using the Berlincourt method) are not capable of deconvoluting the substrate flex from the piezoelectric response of the film and can therefore overestimate the piezoelectric response. The measurements were performed on different electrode sizes (i.e.,  $400 \times 400$   $\mu$ m<sup>2</sup>,  $600 \times 600$   $\mu$ m<sup>2</sup>, and  $800 \times 800$   $\mu$ m<sup>2</sup>) and the effective clamped piezoelectric response  $d_{33,f}$  was calculated based on the procedure described by Sivaramakrishnan *et al.* [68].

The microstructural characterization of AlScN films on structured silicon wafers was performed using a Zeiss Gemini 460 scanning electron microscope (SEM), equipped with a secondary electron (SE) detector operated at an accelerating voltage of 2 kV and a sample current of 50 pA. The samples were cleaved in air and secured onto a SEM sample holder using carbon tape.

#### ACKNOWLEDGMENTS

J.P. acknowledges funding by the SNSF (Project No. 200021\_196980). Bertrand Paviet-Salomon is gratefully acknowledged for providing the structured Si substrates. The authors also acknowledge the help from Sebastian Bette with the DBLI measurements.

J.P. performed conceptualization, investigation, formal analysis, visualization, and writing of the original draft; K.T. performed investigation, and writing, review, and editing; T.S.K. performed investigation and formal analysis; R.K.

performed investigation and formal analysis; and S.S. performed conceptualization, supervision, methodology, formal analysis, visualization, funding acquisition, and writing, review, and editing.

- 
- [1] K. Hashimoto, Thin films deposition for BAW devices, in *RF Bulk Acoustic Wave Filters for Communications* (Artech House, Norwood, MA, 2009), pp. 174–175.
- [2] R. Farrell, High temperature annealing studies on the piezoelectric properties of thin aluminum nitride films, *MRS Proc.* **1052**, 618 (2007).
- [3] M. Akiyama, T. Kamohara, K. Kano, A. Teshigahara, Y. Takeuchi, and N. Kawahara, Enhancement of piezoelectric response in scandium aluminum nitride alloy thin films prepared by dual reactive cosputtering, *Adv. Mater.* **21**, 593 (2009).
- [4] Y. Lu, Development and characterization of piezoelectric AlScN-based alloys for electroacoustic applications, Ph.D. thesis, Universität Freiburg, 2019, 10.6094/UNIFR/149771.
- [5] A. Žukauskaitė, Editorial for special issue “piezoelectric aluminium scandium nitride (AlScN) thin films: Material development and applications in microdevices”, *Micromachines* **14**, 1067 (2023).
- [6] N. Q. Khánh, Z. E. Horváth, Z. Zolnai, P. Petrik, L. Pósa, and J. Volk, Effect of process parameters on co-sputtered  $\text{Al}_{(1-x)}\text{Sc}_x\text{N}$  layer’s properties: Morphology, crystal structure, strain, band gap, and piezoelectricity, *Mater. Sci. Semicond. Process.* **169**, 107902 (2024).
- [7] Y. Zou, Design, fabrication, and characterization of aluminum scandium nitride-based thin film bulk acoustic wave filter, *J. Microelectromech. Syst.* **32**, 263 (2023).
- [8] C. S. Sandu, Abnormal grain growth in AlScN thin films induced by complexion formation at crystallite interfaces, *Phys. Status Solidi* **216**, 1800569 (2019).
- [9] O. Zywitzki, T. Modes, S. Barth, H. Bartzsch, and P. Frach, Effect of scandium content on structure and piezoelectric properties of AlScN films deposited by reactive pulse magnetron sputtering, *Surf. Coatings Technol.* **309**, 417 (2017).
- [10] L. Lapeyre, Deposition and characterisation of c-axis oriented AlScN thin films via microwave plasma-assisted reactive HiPIMS, *Surf. Coatings Technol.* **464**, 129540 (2023).
- [11] C. Höglund, Wurtzite structure  $\text{Sc}_{1-x}\text{Al}_x\text{N}$  solid solution films grown by reactive magnetron sputter epitaxy: Structural characterization and first-principles calculations, *J. Appl. Phys.* **107**, 123515 (2010).
- [12] K. R. Talley, Implications of heterostructural alloying for enhanced piezoelectric performance of (Al,Sc)N, *Phys. Rev. Mater.* **2**, 063802 (2018).
- [13] S. Shao, Z. Luo, Y. Lu, A. Mazzalai, C. Tosi, and T. Wu, High quality co-sputtering AlScN thin films for piezoelectric Lamb-wave resonators, *J. Microelectromech. Syst.* **31**, 328 (2022).
- [14] H. Cui, Three-dimensional printing of piezoelectric materials with designed anisotropy and directional response, *Nat. Mater.* **18**, 234 (2019).
- [15] A. T. Tran, O. Wunnicke, G. Pandraud, M. D. Nguyen, H. Schellevis, and P. M. Sarro, Slender piezoelectric cantilevers of high quality AlN layers sputtered on Ti thin film for MEMS actuators, *Sensors Actuators A Phys.* **202**, 118 (2013).
- [16] E. Österlund, H. Seppänen, K. Bespalova, V. Miikkulainen, and M. Paulasto-Kröckel, Atomic layer deposition of AlN using atomic layer annealing—Towards high-quality AlN on vertical sidewalls, *J. Vac. Sci. Technol. A* **39**, 032403 (2021).
- [17] E. Österlund, S. Suihkonen, G. Ross, A. Torkkeli, H. Kuisma, and M. Paulasto-Kröckel, Metalorganic chemical vapor deposition of aluminum nitride on vertical surfaces, *J. Cryst. Growth* **531**, 125345 (2020).
- [18] M. Akiyama, T. Tabaru, K. Nishikubo, A. Teshigahara, and K. Kano, Preparation of scandium aluminum nitride thin films by using scandium aluminum alloy sputtering target and design of experiments, *J. Ceram. Soc. Jpn.* **118**, 1166 (2010).
- [19] S. Barth, T. Schreiber, S. Cornelius, O. Zywitzki, T. Modes, and H. Bartzsch, High rate deposition of piezoelectric AlScN films by reactive magnetron sputtering from AlSc alloy targets on large area, *Micromachines* **13**, 1561 (2022).
- [20] S. Mertin, Piezoelectric and structural properties of c-axis textured aluminium scandium nitride thin films up to high scandium content, *Surf. Coatings Technol.* **343**, 2 (2018).
- [21] N. Wolff,  $\text{Al}_{1-x}\text{Sc}_x\text{N}$  thin films at high temperatures: Sc-dependent instability and anomalous thermal expansion, *Micromachines* **13**, 1282 (2022).
- [22] J. Su, Growth of highly c-axis oriented AlScN films on commercial substrates, *Micromachines* **13**, 783 (2022).
- [23] Q. Zhang, Deposition, characterization, and modeling of scandium-doped aluminum nitride thin film for piezoelectric devices, *Materials (Basel)* **14**, 6437 (2021).
- [24] M. Gillinger, K. Shaposhnikov, T. Knobloch, M. Schneider, M. Kaltenbacher, and U. Schmid, Impact of layer and substrate properties on the surface acoustic wave velocity in scandium doped aluminum nitride based SAW devices on sapphire, *Appl. Phys. Lett.* **108**, 231601 (2016).
- [25] S. Leone, J. Ligl, C. Manz, L. Kirste, T. Fuchs, H. Menner, M. Prescher, J. Wiegert, A. Žukauskaitė, R. Quay, and O. Ambacher, Metal-organic chemical vapor deposition of aluminum scandium nitride, *Phys. Status Solidi Rapid Res. Lett.* **14**, 1900535 (2020).
- [26] Lam Research, Lam Research Introduces Breakthrough Deposition Technique to Enable Next-Generation MEMS for 5G and Beyond, <https://newsroom.lamresearch.com/2024-03-26-Lam-Research-Introduces-Breakthrough-Deposition-Technique-to-Enable-Next-Generation-MEMS-for-5G-and-Beyond>.
- [27] K. A. Aissa, AlN films deposited by dc magnetron sputtering and high power impulse magnetron sputtering for SAW applications, *J. Phys. D. Appl. Phys.* **48**, 145307 (2015).
- [28] J. Patidar, Improving the crystallinity and texture of oblique-angle-deposited AlN thin films using reactive synchronized HiPIMS, *Surf. Coatings Technol.* **468**, 129719 (2023).
- [29] T. Shimizu, Low temperature growth of stress-free single phase  $\alpha$ -W films using HiPIMS with synchronized pulsed substrate bias, *J. Appl. Phys.* **129**, 155305 (2021).
- [30] M. M. S. Villamayor, Low temperature ( $T_s/T_m < 0.1$ ) epitaxial growth of HfN/MgO(001) via reactive HiPIMS with metal-ion



- synchronized substrate bias, *J. Vac. Sci. Technol. A* **36**, 061511 (2018).
- [31] T. Shimizu, H. Komiya, Y. Teranishi, K. Morikawa, H. Nagasaka, and M. Yang, Pressure dependence of (Ti, Al)N film growth on inner walls of small holes in high-power impulse magnetron sputtering, *Thin Solid Films* **624**, 189 (2017).
- [32] L. Chunwei, Study on vanadium films deposited on concave object by conventional direct current and high power pulsed magnetron sputtering, *Rare Met. Mater. Eng.* **42**, 2437 (2013).
- [33] M. Balzer and M. Fenker, Three-dimensional thickness and property distribution of TiC films deposited by DC magnetron sputtering and HIPIMS, *Surf. Coatings Technol.* **250**, 37 (2014).
- [34] H. Luo, F. Gao, and A. Billard, Effect of auxiliary magnetic field on the conformal coverage of the microtrenches in high power impulse magnetron sputtering, *J. Mater. Process. Technol.* **283**, 116732 (2020).
- [35] A. Ghailane, M. Makha, H. Larhlimi, and J. Alami, Design of hard coatings deposited by HiPIMS and dcMS, *Mater. Lett.* **280**, 128540 (2020).
- [36] E. Lewin, D. Loch, A. Montagne, A. P. Ehasarian, and J. Patscheider, Comparison of Al-Si-N nanocomposite coatings deposited by HIPIMS and DC magnetron sputtering, *Surf. Coatings Technol.* **232**, 680 (2013).
- [37] V. Sittinger, O. Lenck, M. Vergöhl, B. Szyszka, and G. Bräuer, Applications of HIPIMS metal oxides, *Thin Solid Films* **548**, 18 (2013).
- [38] G. Greczynski, Metal versus rare-gas ion irradiation during  $Ti_{1-x}Al_xN$  film growth by hybrid high power pulsed magnetron/dc magnetron co-sputtering using synchronized pulsed substrate bias, *J. Vac. Sci. Technol. A* **30**, 061504 (2012).
- [39] S. Fichtner, N. Wolff, F. Lofink, L. Kienle, and B. Wagner, AlScN: A III-V semiconductor based ferroelectric, *J. Appl. Phys.* **125**, 114103 (2019).
- [40] K. Hirata, K. Shobu, H. Yamada, M. Uehara, S. A. Anggraini, and M. Akiyama, Thermodynamic assessment of the Al-Sc-N ternary system and phase-separated region of the strained wurtzite phase, *J. Eur. Ceram. Soc.* **40**, 5410 (2020).
- [41] M. L. Green, Fulfilling the promise of the materials genome initiative with high-throughput experimental methodologies, *Appl. Phys. Rev.* **4**, 011105 (2017).
- [42] A. Anders, Tutorial: Reactive high power impulse magnetron sputtering (R-HiPIMS), *J. Appl. Phys.* **121**, 171101 (2017).
- [43] J. M. Niewehuizen and H. B. Haanstra, Microfractography of thin films, *Philips Tech. Rev.* **27**, 87 (1966).
- [44] A. Wiczorek, A. G. Kuba, J. Sommerhäuser, L. N. Caceres, C. M. M. Wolff, and S. Siol, Advancing high-throughput combinatorial aging studies of hybrid perovskite thin-films via precise automated characterization methods and machine learning assisted analysis, *J. Mater. Chem. A* **12**, 7025 (2024).
- [45] See Supplemental Material at <http://link.aps.org/supplemental/10.1103/PhysRevMaterials.8.095001> for more information on XRD/XPS characterizations and residual stress evaluation.
- [46] K. M. Green, D. B. Hayden, D. R. Juliano, and D. N. Ruzic, Determination of flux ionization fraction using a quartz crystal microbalance and a gridded energy analyzer in an ionized magnetron sputtering system, *Rev. Sci. Instrum.* **68**, 4555 (1997).
- [47] M. M. Hawkeye and M. J. Brett, Glancing angle deposition: Fabrication, properties, and applications of micro- and nanostructured thin films, *J. Vac. Sci. Technol. A* **25**, 1317 (2007).
- [48] H. Jin, Influence of substrate temperature on structural properties and deposition rate of AlN thin film deposited by reactive magnetron sputtering, *J. Electron. Mater.* **41**, 1948 (2012).
- [49] C. S. Sandu, Impact of negative bias on the piezoelectric properties through the incidence of abnormal oriented grains in  $Al_{0.62}Sc_{0.38}N$  thin films, *Thin Solid Films* **697**, 137819 (2020).
- [50] M. Akiyama, K. Nagao, N. Ueno, H. Tateyama, and T. Yamada, Influence of metal electrodes on crystal orientation of aluminum nitride thin films, *Vacuum* **74**, 699 (2004).
- [51] D. Holec, F. Rovere, P. H. Mayrhofer, and P. B. Barna, Pressure-dependent stability of cubic and wurtzite phases within the TiN-AlN and CrN-AlN systems, *Scr. Mater.* **62**, 349 (2010).
- [52] S. Liu, Stress-dependent prediction of metastable phase formation for magnetron-sputtered  $V_{1-x}Al_xN$  and  $Ti_{1-x}Al_xN$  thin films, *Acta Mater.* **196**, 313 (2020).
- [53] G. Greczynski, S. Mráz, J. M. Schneider, and L. Hultman, Metal-ion subplantation: A game changer for controlling nanostructure and phase formation during film growth by physical vapor deposition, *J. Appl. Phys.* **127**, 180901 (2020).
- [54] Z. Huang, Q. Zhang, S. Corkovic, R. Dorey and R. W. Whatmore, Comparative measurements of piezoelectric coefficient of PZT films by berlincourt, interferometer, and vibrometer methods, *IEEE Transactions on Ultrasonics, Ferroelectrics, and Frequency Control* **53**, 2287 (2006).
- [55] A. L. Kholkin, C. Wüthrich, D. V. Taylor, and N. Setter, Interferometric measurements of electric field-induced displacements in piezoelectric thin films, *Rev. Sci. Instrum.* **67**, 1935 (1996).
- [56] K. Tsubouchi, K. Sugai, and N. Mikoshiba, AlN material constants evaluation and SAW properties on AlN/ $Al_2O_3$  and AlN/Si, in *1981 Ultrasonics Symposium* (IEEE, New York, 1981), pp. 375–380.
- [57] S. Mertin, Non-destructive piezoelectric characterisation of Sc doped aluminium nitride thin films at wafer level, in *Proceedings of the 2019 IEEE International Ultrasonics Symposium (IUS)* (IEEE, New York, 2019), pp. 2592–2595.
- [58] M. A. Caro, Piezoelectric coefficients and spontaneous polarization of ScAlN, *J. Phys. Condens. Matter* **27**, 245901 (2015).
- [59] S. Mertin, B. Heinz, A. Mazzalar, T. Schmitz-Kempen, S. Tiedke, and T. Pensala, High-volume production and non-destructive piezo-property mapping of 33% SC doped aluminium nitride thin films, in *Proceedings of the 2018 IEEE International Ultrasonics Symposium (IUS), Kobe, Japan* (IEEE, Piscataway, NJ, 2018), pp. 1–4.
- [60] S. Mertin, Enhanced piezoelectric properties of c-axis textured aluminium scandium nitride thin films with high scandium content: Influence of intrinsic stress and sputtering parameters, in *Proceedings of the 2017 IEEE International Ultrasonics Symposium (IUS), Washington, D.C., USA* (IEEE, Piscataway, NJ, 2017), pp. 1–4.
- [61] T. Sgrilli, A. Azzopardi, V. Bellido-Gonzalez, D. Monaghan, I. Fernández, and A. Wennberg, Conformal coatings deposited on microstructured substrates using HiPIMS and a full face erosion cathode, in *SVC TechCon* (Society of Vacuum Coaters (SVC), Long Beach, CA, 2019). <https://www.gencoa.com/resources/documents/PP3-Sgrilli-Hipims.pdf>

- [62] L. Jablonka, P. Moskovkin, Z. Zhang, S.-L. Zhang, S. Lucas, and T. Kubart, Metal filling by high power impulse magnetron sputtering, *J. Phys. D: Appl. Phys.* **52**, 365202 (2019).
- [63] S. Zhuk, Combinatorial reactive sputtering with auger parameter analysis enables synthesis of wurtzite  $\text{Zn}_2\text{TaN}_3$ , *Chem. Mater.* **35**, 7069 (2023).
- [64] S. Zhuk, Synthesis and characterization of the ternary nitride semiconductor  $\text{Zn}_2\text{VN}_3$ : Theoretical prediction, combinatorial screening, and epitaxial stabilization, *Chem. Mater.* **33**, 9306 (2021).
- [65] M. Akiyama, T. Kamohara, K. Kano, A. Teshigahara, and N. Kawahara, Influence of oxygen concentration in sputtering gas on piezoelectric response of aluminum nitride thin films, *Appl. Phys. Lett.* **93**, 021903 (2008).
- [66] L. Vergara, Influence of oxygen and argon on the crystal quality and piezoelectric response of AlN sputtered thin films, *Diam. Relat. Mater.* **13**, 839 (2004).
- [67] X. Zhu, X. Chen, H. Liu, R. Kang, B. Zhang, and Z. Dong, An empirical equation for prediction of silicon wafer deformation, *Mater. Res. Express* **4**, 065904 (2017).
- [68] S. Sivaramakrishnan, P. Mardilovich, T. Schmitz-Kempen, and S. Tiedke, Concurrent wafer-level measurement of longitudinal and transverse effective piezoelectric coefficients ( $d_{33,f}$  and  $e_{31,f}$ ) by double beam laser interferometry, *J. Appl. Phys.* **123**, 014103 (2018).